Mass-transfer based modeling to investigate iodine staining effects for enhanced contrast X-ray computed tomography

Zhi-Heng Li [a,b,*], Fei Yan [c], Richard A. Ketcham [d], Matthew W. Colbert [d], Julia A. Clarke [d]

[a] *Key Laboratory of Vertebrate Evolution and Human Origins, Institute of Vertebrate Paleontology and Paleoanthropology, Chinese Academy of Sciences, Beijing 100044, China*
[b] *CAS Center for Excellence in Life and Paleoenvironment, Beijing 100044, China*
[c] *Department of Civil and Environmental Engineering, Rice University, Houston, TX, USA*
[d] *Department of Geological Sciences, University of Texas at Austin, Austin, TX, USA*

Abstract

Iodine staining combined with X-ray computed tomography (CT) has become a core approach in anatomy, offering three-dimensional and essentially non-destructive imaging of soft tissues. Although there have been rapid advances in methodologies and techniques, the mechanisms underlying diffusible iodine contrast-enhanced CT are not yet fully understood. The protocols for staining samples of differing sizes and tissue types have not yet been justified theoretically. Here we utilize mass transfer modeling to simulate iodine diffusion and predict iodine concentrations within distinct tissue types. We also undertake iodine staining experiments to visualize the detailed anatomy and contrast effects on whole-body avian specimens using different concentrations of iodine solution to compare with model simulation results. The simulations effectively explain most observed concentration changes in differently-sized samples over distinct iodine treatment durations. These results also provide insight into the mechanisms behind the efficacy of solution replenishment for enhancing staining effects. Both consistencies and inconsistencies between our simulation and experimental results regarding iodine concentration in tissues will inform further investigations to optimize iodine staining protocols.
© 2018 Elsevier Ireland Ltd Elsevier B.V. and Nanjing Institute of Geology and Palaeontology, CAS. Published by Elsevier B.V. All rights reserved.

1. Introduction

DiceCT (diffusible iodine contrast-enhanced computed tomography) has been used to image a diversity of specimens including flowers, tiny insects, isolated organs and whole bodies ranging in size from embryos to large vertebrates (Aslanidi et al., 2013; Holliday et al., 2013; Li et al., 2015, 2016; Gignac et al., 2016). The new method is becoming an essential tool in anatomical studies, and has the potential to advance other disciplines such as functional morphology (Holliday et al., 2013; Herdina et al., 2015; Kupczik et al., 2015). Although the num-

ber of published studies using diceCT has increased rapidly, the rationales for particular staining protocols have not been explicitly defined for different types of specimens (Metscher, 2009a, 2009b; Gignac et al., 2016). Operationally, it is often personal preference and experience that have influenced what specific protocol is applied to a specimen, in part due to a limited understanding of the physical and chemical mechanisms of iodine staining (Lecker et al., 1997).

During diffusion-based staining, iodine concentration and staining duration are the most critical parameters that need to be validated and optimized (Tahara and Larsson, 2013; Gignac et al., 2016; Li et al., 2016). Iodine species travel across the solution-specimen boundary (often comprising integument in whole organisms), move into the specimen, and bind with distinct tissues differently (Li et al., 2015). Because of the complex reactions between iodine and different tissues, it has been dif-

* Corresponding author at: Key Laboratory of Vertebrate Evolution and Human Origins, Institute of Vertebrate Paleontology and Paleoanthropology, Chinese Academy of Sciences, Beijing 100044, China.
  E-mail address: lizhiheng@ivpp.ac.cn (Z.H. Li).

ficult to optimize staining protocols for different specimens or studies (Tahara and Larsson, 2013). Practical problems commonly encountered in staining include both over-staining and insufficient staining as a consequence of inappropriate staining duration and/or iodine concentration (Jeffery et al., 2011; Gignac et al., 2016). This can complicate identification, visualization, and interpretation of the investigated anatomy. Solving these problems requires better understanding of the relationship between quantitative contrast; iodine concentration, penetration, and adsorption; and staining duration — a relationship that is poorly understood and only briefly addressed in previous studies (Faulwetter et al., 2013; Wong et al., 2013; Gignac and Kley, 2014; Gignac et al., 2016).

The staining process can be explained as a specialized form of mass transfer (Cussler, 2009). Chemical potentials or gradients are the major driving force for movement of the iodine molecules from solution to tissues (Cussler, 2009). During the staining process, the concentration of iodine in the tissues increases and the boundary flux decreases because of a reduced concentration gradient (Li et al., 2015). This effect can be counteracted by replenishing the iodine staining solution (Li et al., 2015; Gignac et al., 2016). Precise control of iodine infiltration into sample tissues is important for optimizing CT imaging; undesirable effects of poor staining include overstaining, shrinkage and/or uneven staining of tissues (Wong et al., 2013; Gignac et al., 2016). Accordingly, an accurate estimate of both the iodine concentration and boundary flux is critical to understanding the particular type of mass transfer behind the staining mechanism. Relevant quantitative modeling has been limited and has not been used to determine staining protocols for particular specimens (Tahara and Larsson, 2013). There are also limited quantitative studies to inform adjustment of the iodine concentration for different sample sizes and types (Degenhardt et al., 2010). Fewer studies have presented detailed comparison of different staining protocols and the comparative advantages and disadvantages of specific treatments (Gignac et al., 2016; Li et al., 2016).

Here mass transfer modeling is used as an analytic tool to examine the staining results and iodine concentrations within tissues over the staining period. Decreased driving force (Cussler, 2009) may explain the effect of solution replacement from this perspective. We firstly test whether mass transfer modeling is efficient and accurate for predicting the observed concentration change in muscle tissues during staining. Simulations are carried out to validate the mass transfer coefficients independently within the three samples. We further define an "Effectiveness Factor" (η, Eq. (13) in Section 2.1) to evaluate when and how to replenish the staining solution during long staining periods. Finally, we propose a theoretical basis derived from these simulations to inform best practices in iodine staining. We present progressive staining experiments of whole-bodied avian specimens of different sizes using different treatments and use simulations to explore the potential mechanisms behind the diceCT results. An integrated analysis that combines modeling with different experimental designs is used to address problems encountered in staining experiments. This novel method presents an avenue for experimental biologists to investigate similar problems. Practically, the present work also provides a model for characterizing and visualizing avian anatomy in a convenient and affordable way.

2. Materials and methods

2.1. Simulation

The model used to describe the iodine staining process in this study is based on mass transfer theory (Cussler, 2009). Diffusion and sorption are the two processes by which iodine molecules move through and bind with tissues during the staining process. The staining process can be explained using a mass transfer coefficient as a simple and effective descriptor. The mass transfer concept facilitates the analysis and provides more flexibility for modeling diffusion processes involving molecule transport across interfaces.

A simplified one-dimensional diffusion–sorption (D–S) model describes the transport and binding of iodine in the tissue. For the sorption process, it is assumed that the sorption isotherm is linear. The governing equation is as follows:

$$(\theta + \rho_b K_d) \frac{\partial c}{\partial t} = \theta D \frac{\partial^2 c}{\partial x^2} \tag{1}$$

where $c(x, t)$ is the concentration of iodine in the solute phase (mmol/l), θ is porosity (0–1), ρ_b is bulk density (kg/l), D is the diffusion coefficient (m^2/s), and the partition coefficient K_d describes the sorption of iodine between solid phase (tissue) and solute phase (i.e., $K_d = c_{solid}/c$ with units of l/kg). The retardation factor R_f is defined as $(1 + \rho_b K_d/\theta)$, and Eq. (1) simplifies to

$$\frac{\partial c}{\partial t} = \frac{D}{R_f} \frac{\partial^2 c}{\partial x^2} \tag{2}$$

The initial condition of iodine in the sample can be specified not only for non-treated samples, which have zero iodine, but also for samples having any pre-existing spatially varied concentration.

$$c(x, 0) = f(x) \tag{3}$$

We use a one-dimensional model with length L (m) and specify two boundary conditions.

At the outer boundary ($x = 0$), iodine enters the tissue driven by the concentration gradient between the bulk solution of staining iodine and solution in the tissue. In previous studies, either a constant concentration or constant flux boundary condition has been specified at the solution-tissue interface (Degenhardt et al., 2010; Li et al., 2015, 2016). Because of mass transfer resistance, however, iodine at the boundary in the tissue cannot establish the same concentration as in the bulk solution over a short time span, and a constant concentration boundary condition is not appropriate. While a constant flux boundary condition works well for short staining durations (e.g., a few days), it does not account for the decrease in the concentration gradient at the interface as iodine concentration increases in the tissue with

time. Accordingly, we propose a more general mass transfer boundary condition at the interface ($x = 0$):

$$-\theta D \frac{\partial c}{\partial x} = k_m (c_b - c), \quad x = 0 \tag{4}$$

where c_b is iodine concentration in the bulk solution outside the boundary (mmol/l), and k_m is a mass transfer coefficient (m/s). Mathematically, this is known as the Robin boundary condition or third type boundary condition. It is a specification of a linear combination of the values of a function and the values of its derivative on the boundary of the domain (Kevorkian, 1990).

The inner boundary ($x = L$), is in the interior of the whole specimen and the flux is negligible, so a zero flux boundary condition is specified:

$$\frac{\partial c}{\partial x} = 0, \quad x = L \tag{5}$$

The details for solving Eq. (1) or (2) with initial condition Eq. (3) and boundary conditions of Eqs. (4) and (5) can be found in Appendix A in Supplementary material. The final solution for $c(x,t)$ is

$$c = c_b \left[1 - \sum_{n=1}^{\infty} q_n * \exp\left(-\frac{u_n^2 Dt}{R_f L^2}\right) * \cos\left(u_n \left(1 - \frac{x}{L}\right)\right) \right] \tag{6}$$

where

$$q_n = \frac{\int_0^1 g(Z) \cos(u_n Z)\, dZ}{\int_0^1 \cos^2(u_n Z)\, dZ} \tag{7}$$

u_n is the positive root of

$$u_n \tan(u_n) - \frac{k_m L}{\theta D} = 0 \tag{8}$$

and $g(x)$ is related to initial condition Eq. (3) by the following equation:

$$g(x) = 1 - \frac{f(L(1-x))}{c_b} \tag{9}$$

The total concentration in the tissue $c_T(x,t)$ is expressed as follows:

$$c_T = \theta R_f c = \theta R_f c_b \left[1 - \sum_{n=1}^{\infty} q_n * \exp\left(-\frac{u_n^2 Dt}{R_f L^2}\right) \right.$$
$$\left. * \cos\left(u_n \left(1 - \frac{x}{L}\right)\right) \right] \tag{10}$$

The average total concentration in space in the tissue $c_{Tavg}(t)$ is

$$c_{Tavg} = \theta R_f c_b \left[1 - \sum_{n=1}^{\infty} q_n * \exp\left(-\frac{u_n^2 Dt}{R_f L^2}\right) * \frac{\sin(u_n)}{u_n} \right] \tag{11}$$

If there is no iodine in the sample at $t = 0$, i.e., $c(x,0) = 0$, coefficient q_n can be simplified to

$$q_n = \frac{2\sin(u_n)}{u_n + \sin(u_n)\cos(u_n)} \tag{12}$$

The staining effectiveness factor $\eta(t)$ is defined as the influx of iodine at time t over the influx at time $t = 0$. Because of the concentration increase in the tissue at the boundary, $\eta(t)$ decreases over time. When it drops below a threshold value of η_c replenishing the staining reagent is indicated.

$$\eta = \sum_{n=1}^{\infty} q_n * \exp\left(-\frac{u_n^2 Dt}{R_f L^2}\right) * \cos(u_n) \tag{13}$$

This analytical solution requires the calculation of an infinite number of eigenvalues u_n ($n = 1, 2, 3, \ldots$), which are positive roots of Eq. (8). These roots u_n have the following pattern:

$$u_1 \in (0, \pi), \quad u_2 \in (\pi, 2\pi), \quad u_3 \in (2\pi, 3\pi), \ldots,$$
$$u_k \in ((k-1)\pi, k\pi), \ldots \tag{14}$$

These "u_n" are present in the exponential term exp$[-u_n^2 Dt/(R_f L^2)]$, so the significance of each eigenvalue u_n decreases with increasing n and t. For a short staining period (a few days), a large number of u_n (e.g., u_{20}) may be required, but only a few can be used without loss of accuracy for longer times. As shown in the supplemental file, only four u_n terms were needed to produce highly accurate results for the staining of three specimens (*Progne subis*, *Archilochus alexandri*, and *Melanerpes aurifrons*) used in this study.

2.2. Experimental design and concentration acquisition

Three independent staining experiments were carried out at The University of Texas at Austin, Vertebrate Paleontology Laboratory. Birds were chosen for these tests because they are underrepresented in anatomical references relative to other vertebrates (Diogo and Abdala, 2010). The specimens comprised a Golden-Fronted Woodpecker (*M. aurifrons* TMM M-16042) a Black-Chinned Hummingbird (*A. alexandri* TMM M-16038), and a Purple Martin (*P. subis* TMM M-16625). The specimens were salvaged under Federal Bird Permit (MB52556B-0) in late 2015. They were frozen at $-23\,°C$ (or $-10\,°F$) for a few months before the experiment began in early 2016.

The *A. alexandri* specimen measures about 6 cm from bill to tail, and around 2 cm for its maximal thoracic diameter. The *P. subis* specimen is ~12 cm in length and 5 cm in maximal thoracic diameter. The larger *M. aurifrons* specimen is ~16 cm in length and is 5–6 cm in maximal thoracic diameter. The *A. alexandri* specimen was fixed using 10% neutral buffered formalin (NBF) for eight days, and then transferred to 70% ethanol for further fixation for another eight days (Hopwood, 2002). The specimen was stained using 1% iodine–ethanol-formalin solution (1 g I$_2$/75 ml absolute ethanol [200 proof Ethanol] and 25 ml 10% neutral buffered formalin) for 16 days. The larger-sized *P. subis* was fixed in 650 ml 10% NBF for three days and then the solution was changed to ethanol-formalin (325 ml 10% NBF and 325 ml 70% ethanol) for five days. The *P. subis* specimen was then transferred to another ethanol-formalin solution (150 ml 10% NBF and 450 ml 70% ethanol) for 11 days. The specimen was scanned first as a control prior to staining and before transfer

Table 1
Scanning parameters (e.g., voltage, current, and power) used in the experiment.

Scanning paramete	*P. subis* scan 0	*P. subis* scan 1	*P. subis* scan 2	*A. alexandri*	*M. aurifrons* scan 1	*M. aurifrons* scan 2
Voltage (kV)	150	150	150	150	180	180
Current (mA)	0.2	0.2	0.2	0.19	0.3	0.3
Source to object (mm)	197.687	197.7	197.7	145.0	223.551	227.0
Source to detector (mm)	1316.589	1316.877	1316.774	1316.774	1316.772	1316.772
Vertical extent (mm)	136.9	135.6	171.3	65.5	175.1	178.0
Voxel size (mm)	0.0479	0.0479	0.048	0.0241	0.0597	0.0614

Table 2
Inter-calibration of pixel intensity (grayscale values) to account for beam-hardening and helical artifacts that caused variation across the different scans. Corrected values calculated from raw values as $(CT_{raw} - Air_{raw}) \times (Range_{avg}/Range_{raw}) + Air_{avg}$. The *P. subis* and *M. aurifrons* were calibrated separately.

Scan	Uncorrected grayscale value (raw)			Average grayscale value (avg)		
	Air	Fixed solution (in a vial scanned)	Range (solution–air)	Air	Fixed solution	Range (solution–air)
Non-stain (scan 0)	5141	18,200	13,059	6683.7	15,308.3	8624.7
P. subis scan 1	8010	17,525	9515			
P. subis scan 2	6900	10,200	3300			
M. aurifrons scan 1	9560.8	20,754.5	11,193.7	6953.3	16,579.4	9626.1
M. aurifrons scan 2	4345.8	12,404.3	8058.5			

of the specimen to 70% ethanol for three days. The *P. subis* specimen was then progressively stained with three concentrations of iodine–ethanol-formalin solution. In the first stage, 1% iodine solution (6 g I_2/150 ml 10% NBF and 450 ml absolute ethanol [200 proof Ethanol] was used for 25 days. In the second stage 2% (12 g I_2/150 ml 10% NBF and 450 ml ethanol [200 proof Ethanol]) iodine concentrations were used for 21 days, and then 3% (18 g I_2/150 ml 10% NBF and 450 ml absolute ethanol [200 proof Ethanol]) iodine concentrations was used for 18 days. The *M. aurifrons* specimen was fixed in 650 ml 10% NBF for nine days, and then transferred to 70% ethanol. It was preserved in 70% ethanol for about two months. For the first stage staining, 2% solution 12 g I_2/(480 ml [200 proof Ethanol] + 160 ml 10% NBF) was used for 27 days; after solution replacement (with a 2% solution), the second stage staining was conducted for another 27 days, and the total staining period was 54 days.

The CT scans were completed at the University of Texas High-Resolution X-ray CT facility (UTCT) using a scanner custom-built by North Star Imaging, Inc., Rogers, MN USA. Scan parameters are provided in Table 1. The three scans (numbered as scan 0, 1 and 2) of the *P. subis* specimen (after fixation, after the first stage of staining, and after the second stage of staining) included a vial of fixing solution (1 ml NBF and 3 ml 70% ethanol) in the field of view to aid in calibration. For the *A. alexandri*, since only one CT scan was obtained after the single staining duration, no post-calibration was applied. For the *M. aurifrons* specimen, two scans were obtained, after the first 27-day staining period and after the second 27-day stage. The fixation and staining duration were determined based on prior experiments (Li et al., 2015, 2016) and size differences. All specimens were scanned within the plastic wrapping in order to prevent evaporation and distortion during the scanning. The pectoral region, with its large muscle masses, was used to measure the CT grayscales (in 16-bit Tiff images) and transform the data

to iodine concentration for the mass transfer modeling described as follows.

2.3. Grayscale values — iodine concentration conversion

Data for experimental calibration and simulation was acquired from a cross-section from the sternal muscle. Grayscale values were firstly measured in ImageJ v1.48, and then calibrated across the three *P. subis* scans and the two *M. aurifrons* scans; see Table 2 for calibration equations. Although no calibration was applied between the *P. subis* data and the *M. aurifrons* data, calculated grayscale values for the solution and air were quite close (see Table 2).

Solution trapped in the empty eye orbital space was used as a standard to convert the CT numbers (i.e., the grayscale values) of stained tissues to an "absolute concentration" of iodine. While 1% solution was used, eventually the solution trapped in the eye orbit was approximately 78.8 mmol/l. Because volume of the solution used is much larger than that of the specimen size, the minor difference was ignored here. The iodine concentration of tissue could then be obtained by comparing the ratio of the grayscales of the eye orbit fluid to that measured in the tissues. Similar conversion was used for the staining of *M. aurifrons* and *P. subis* as well (2% iodine solution = 157.6 mmol/l, 3% iodine solution = 236.4 mmol/l).

3. Results

3.1. Soft tissue staining results and bone-muscle contrast

We systematically compared the CT measurements of bone, muscle, fasciae, and nervous tissues at different staining stages for the three specimens shown in Fig. 1. With 1% iodine solution, grayscales for the stained bones of *P. subis* vary from 30,000 to
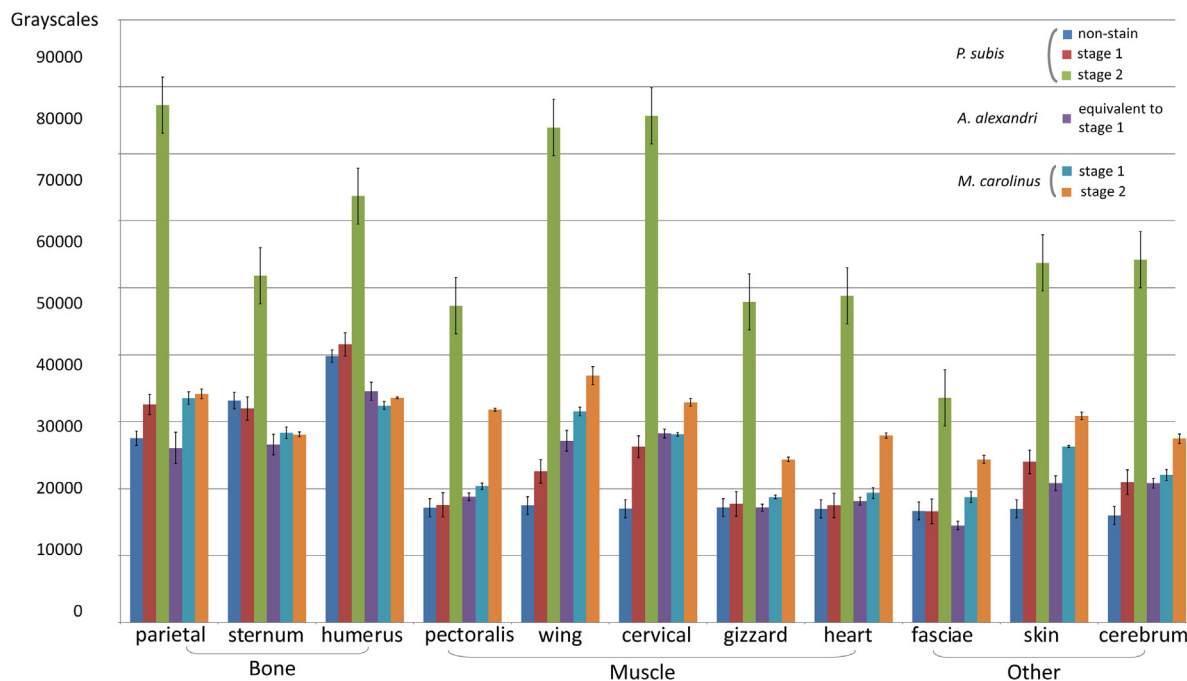
Fig. 1. CT values measured in different tissues before staining, and after two stages of staining in the *P. subis* specimen, one stage staining of the *A. alexandri* specimen, and two stages of *M. aurifrons* staining. Values are means of all pixels selected as reflecting each tissue in ImageJ, and standard deviations are shown as I-bars. CT values for *P. subis* were cross-calibrated as described in Section 2.3. Grayscale values — iodine concentration conversion. The values of skin are an average number for the epidermis and dermis. The fasciae were measured between the skin and the pectoral muscle.

40,000 in the first stage (Fig. 1); similar numbers were obtained in the *M. aurifrons* staining with the application of a 2% solution. The final grayscale values of the stained bones were much higher in *P. subis* than in either *A. alexandri* or *M. aurifrons*, because the iodine solution was continuously enhanced (1%, to 2%, and to 3%).

Grayscale values of muscle tissues vary largely by location and also by the mass of the measured muscle (Fig. 1: Muscle) in both stages (stages 1 and 2) for the three specimens. With a 1% concentration, *P. subis* showed little increase in the CT values of the pectoral, cardiac region, and gizzard muscles (e.g., 17,170–17,722) but large increases in the muscles from the forearm and cervical region (Fig. 1: 17,493–22,558; 17,010–26,266). This was also the case for *M. aurifrons*, where forearm and cervical muscles show much higher grayscale values than other regions. Internal organs and large muscle masses generally showed inadequate penetration of iodine (Figs. 2 and 3). With 2% iodine concentration treatment in the first stage, the grayscale values of muscle in *M. aurifrons* is higher than that of *P. subis*, as seen in the relatively small-sized wing muscles that are located in the closer proximity to the staining solution.

Connective tissues, e.g., fasciae, have much lower grayscales during any staining period compared with other tissues, even the fasciae close to the solution (e.g., under the skin). The lower contrasted fasciae and other connective tissues (blood vessels) help define boundaries between muscular fibers, and the vascular system. These structures are best seen after the second stage of staining when neighboring tissues were highly stained (Figs. 2, 3). In the integument, the keratinous rachis was strongly

stained in the flight feathers, with the lumen of the rachis filling with lower-contrast solution (Fig. 2: rac). This demonstrates potential high adsorption of iodine by keratinized tissues, including the feathers and also beak, tongue and the claws (Fig. 3). The nervous system, such as the cerebrum, is much less stained than its encasing braincase. The cerebrum and cerebellum show distinct differences in contrast.

3.2. Models of concentration profiles

The physical properties of tissues, including bulk density, porosity, partition coefficient, and diffusion coefficient, all affect staining. Based on the parameter set from Li et al. (2015, 2016) (Table 1 in Appendix A in Supplementary material), the resultant calibrated mass transfer coefficients (k_m) were $6.7E - 9$ m/s in *P. subis*, $6.3E - 9$ m/s in the *A. alexandri* and $5.8E - 9$ m/s for the *M. aurifrons* specimen, only differing by about 10% among the three. Even when the solution was replaced twice with higher iodine solution concentrations in the *P. subis* staining, a single mass transfer coefficient was adequate to describe the observed effects. The simulations predict the observed CT values within muscular tissues, or tissue concentration profiles of pectoral muscles, of the *P. subis* specimen at both Day 25 and Day 64 (Fig. 4). However, it only accurately captures one profile of the *M. aurifrons* specimen in the first stage staining at duration of Day 27. The simulated concentration in Day 54 is 10% higher than that measured data in the *M. aurifrons* specimen. Further calculation of the root-mean-square error (RMSE) demonstrates the fitness of model to experiment. The RMSE values are quite small in the early-stage staining in the three specimens and rise
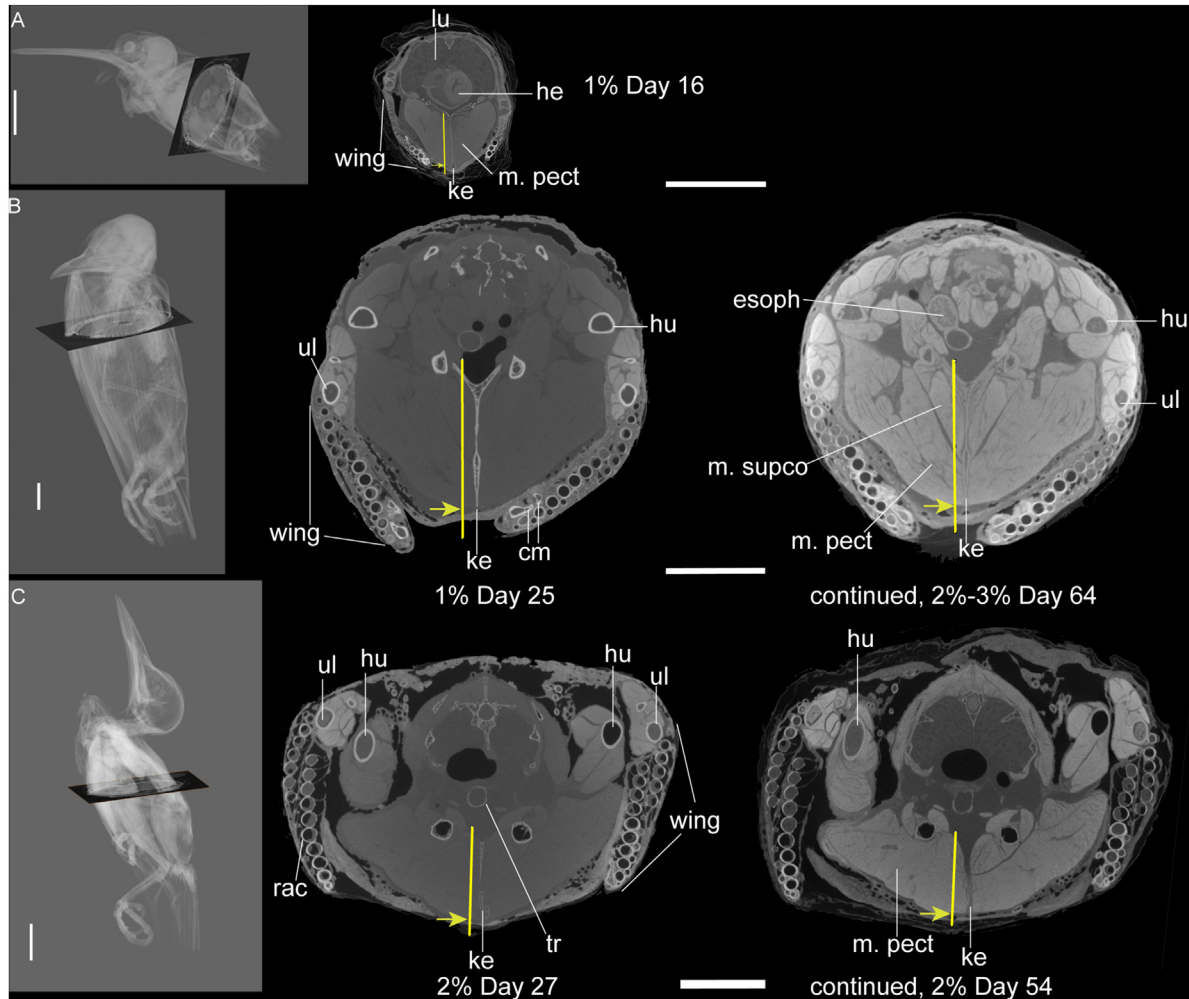
Fig. 2. CT images across the pectoral region of *A. alexandri* (A), *P. subis* (B), and *M. aurifrons* (C). Yellow lines indicate where measurements used for simulation and modeling were acquired. Yellow arrows indicate the start of muscular tissues, corresponding to x (0) for the simulations. Anatomical abbreviations: cm – carpometacarpus, esoph – esophagus, he – heart, hu – humerus, ke – sternal keel, lu – lung, m. pect – m. pectoralis, m. supco – m. supercoracoid, rac – rachis, tr – trachea, ul – ulna. These cross-section images were slightly out of alignment with one another, but the general nature of staining holds; all scale bars equal to 15 mm.

in later stages, although the absolute numbers remain quite low compared to the total concentration: *A. alexandri* (3.5); *P. subis* (3.6 at Day 25 and 19.4 at Day 64); *M. aurifrons* (3.8 at Day 27 and 35.6 at Day 54).

The concentration of iodine in the muscle tissues is about 60–100 mmol/l measured for the first-stage staining in the *A. alexandri* and *P. subis* specimen and approaches 200 mmol/l in the *M. aurifrons* specimen (see Section 2.3). The enhanced effect of multi-stage staining is demonstrated by the average iodine concentration within muscular tissues, which increased from about 100 mmol/l to about 350 mmol/l (Fig. 4A) in the *P. subis* and to about 250–300 mmol/l in *M. aurifrons*. However, the concentration predicted by the simulation was slightly over 300 mmol/l in *M. aurifrons*.

3.3. A quantitative tool to explore the staining process

The proposed **Effectiveness Factor** η (Eq. (13) in Section (2.1)) can be used to evaluate when and how to replenish the staining solution at a given time t (Eq. (10) in Section (2.1)).

The diagram (Fig. 5) describes the progression of staining in the targeted tissues (muscles) with time. As shown in the simulation, $\eta(t)$ drops quickly early in the staining period and levels off eventually (Fig. 2 in Appendix A in Supplementary material). When $\eta(t)$ drops below an empirical value, e.g., 0.6–0.7, which generally suggests the staining power reduces about 30%–40% and replenishing the staining reagent is suggested. Our solution replacement in experiments is quite close to the days (25 versus 27) indicated by the modeling.

We numerically tested four hypothetical scenarios involving different staining strategies (1%, 2%, and 3% respectively). These results were compared to results from progressive enhancement in iodine concentration (1%–3%) applied in the experiment (Fig. 5). In contrast to the step-wise increase of iodine concentration, a gradual increase of the iodine concentration was obtained with final concentrations of iodine about 150 mmol/l, 300 mmol/l, 450 mmol/l respectively for the 1%, 2%, and 3% being modeled. The concentration for the step-wise staining strategy (1% increase to 2%, and then to 3%) used
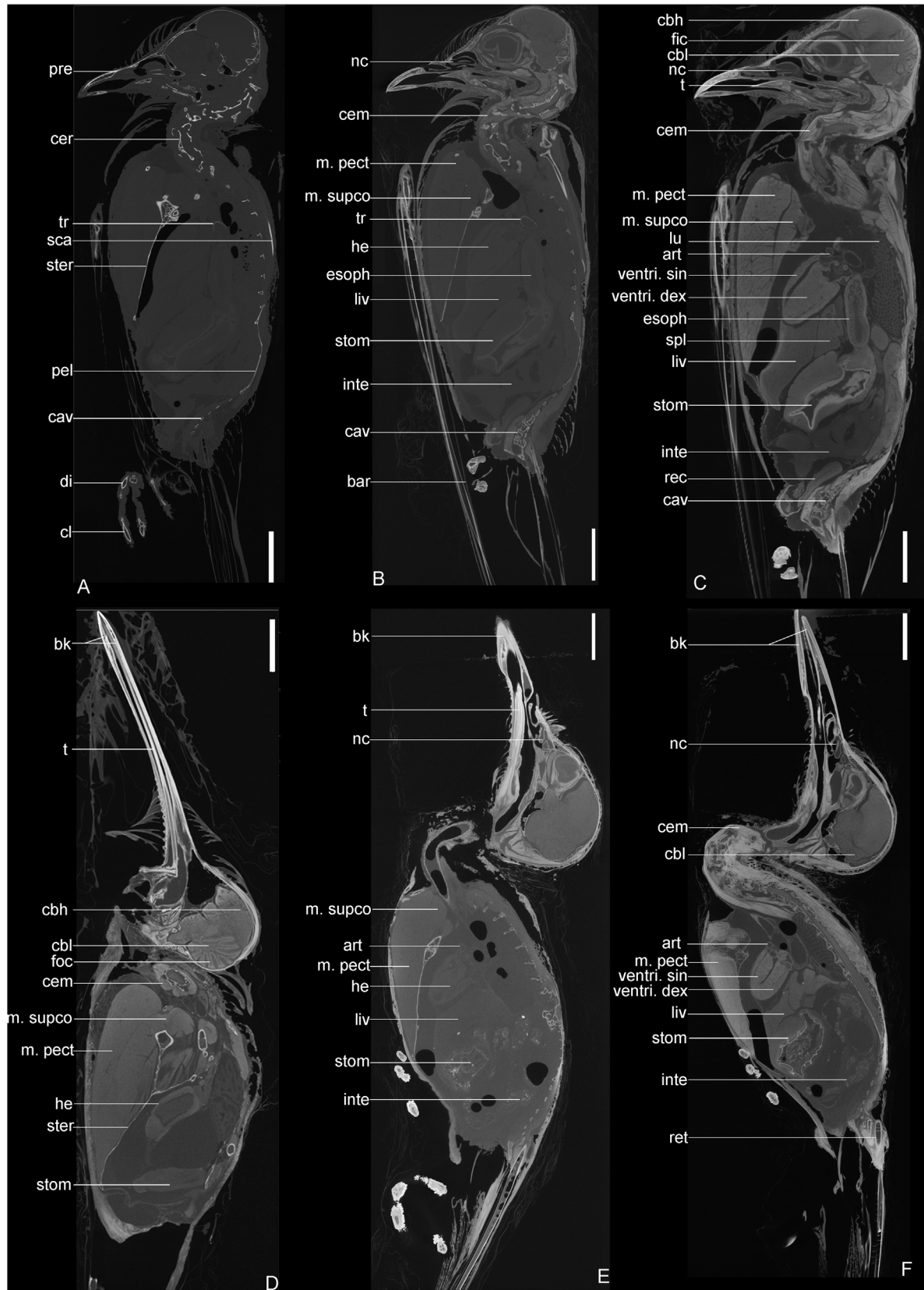
Fig. 3. Sagittal section of *P. subis* (A, B, and C), *A. alexandri* (D), and *M. aurifrons* (E and F) specimen before (A) and after the first stage (B, D, and E), and the second stage of staining (C and F). Anatomical abbreviations: art – artery, bar – barbule, bk – beak, cav – free caudal vertebrate, cbh – cerebral hemisphere, cbl – cerebellum, cem – cervical muscle, cer – cervical, cl – claw, di – digit, esoph – esophagus, fic – fissura cerebelli, foc – folia cerebelli, he – heart, inte – intestine, liv – liver, lu – lung, m. pect – m. pectoralis, m. supco – m. supercoracoid, nc – nasal capsule, pel – pelvis, pre – premaxilla, rec – rectum, ret – retries, sca – scapula, spl – spleen, ster – sternum, stom – stomach, t – tongue, tr – trachea, ventri. dex – ventriculus dexter, ventri. sin – ventriculus sinister. All scale bars equal to 10 mm, except the scale bar in (D) (equal to 4 mm).
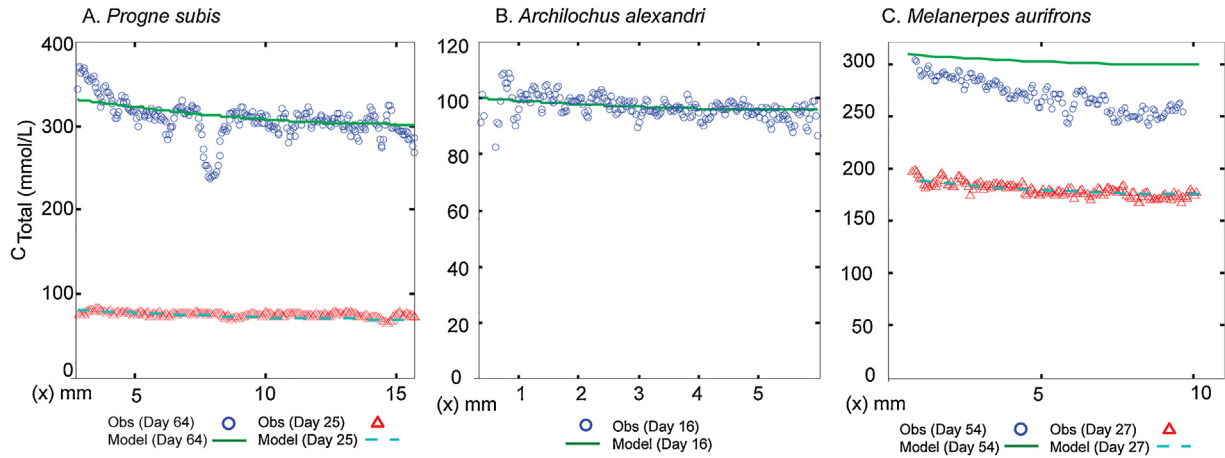
Fig. 4. Model simulation in comparison with experimental observation for *P. subis* staining (A) at Day 25 and Day 64, *A. alexandri* staining at Day 16 (B) and *M. aurifrons* staining (C) at Day 27 and Day 54. Obs and Model represent observation data and modeling fit results respectively. 'X' axis represents the distance of tissue where measurements were taken for the staining depth; 'Y' axis represents the total iodine concentration that converted from grayscale values.
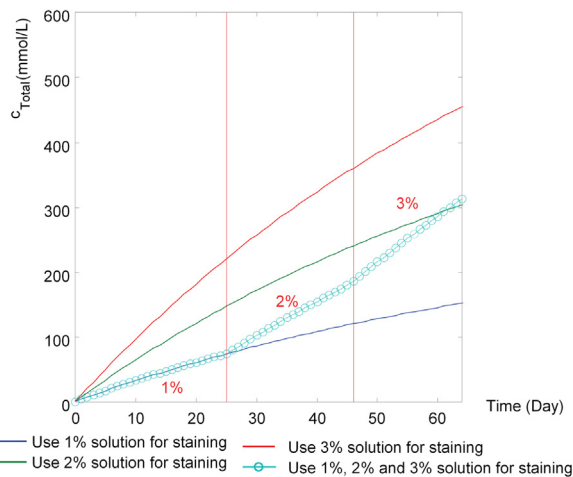

Fig. 5. Model results of average total concentration for *P. subis* staining if using 1%, 2%, and 3% solution throughout the whole process, in comparison with concentration-varied solution (1%, 2% and 3%) used in the experiment.

is slightly higher than that of 2% used throughout the whole duration.

4. Discussion

The mass transfer model presented here is simple in its parameter assumptions and generally accurate for calculating average concentration to predict staining progress. As shown in the modeling, the results provide a good estimate of the iodine concentration profile in the experiment data in the small *A. alexandri* and the larger *P. subis* datasets, and partially for the *M. aurifrons* datasets. Similar values calibrated for the transfer coefficient (k_m) from the three independent experiments indicate that the mass-transfer theory serves well as a uniform law for tracing staining progress, at least within the experimental parameters of concentration and duration explored thus far. This conclusion supports the idea that experiments from one study can be used as a reliable reference for others, as suggested previously (Gignac et al., 2016). The inferences we have gained from exam-

ining avian materials in this study should apply to other iodine staining practices for avian specimens as well.

The final grayscales for muscles generally closely positively correlates to the concentration of the solution applied (Fig. 4). The proportional change of grayscales in the muscular tissues observed in *M. aurifrons* (2%) between the first and the second stage of staining (each 2%) was much less than that of the *P. subis* specimen, suggesting a step-wise increase (1%, to 2%, and to 3%) of concentration plays a key role in contrast enhancement (Fig. 1).

These results provide a validated relationship regarding the contrast effect of muscular tissues that would be obtained for a given iodine concentration and duration for a *P. subis*-sized specimen (Fig. 5). Likewise, the modeling is shown to encompass the effect of incrementally raising the iodine concentration. Mammalian specimens have thick integument (i.e., hairs), dense bones and associated muscular tissues. For the similar-sized mammalian specimens, the protocol should be applicable similarly regarding concentration and timing for staining (Li, unpublished data).

This study demonstrates how mass transfer theory can be used as a tool in understanding the critical role of concentration in affecting staining results. In previous analyses (Degenhardt et al., 2010; Li et al., 2015), a constant flux was assumed at the exterior boundary between solution and the sample; in contrast, the mass transfer modeling here simulates the boundary flux condition in a more realistic way by taking the concentration change into account along with staining progress.

Although our modeling accurately reproduces most of the staining progress, specimen distortion remains an important issue to be considered and resolved. Since a highly concentrated iodine solution contributes to the high degree of distortion and shrinkage to the specimen (Vickerton et al., 2013), we consistently used a lower concentration in prior experiments (Li et al., 2015, 2016). But lower concentrated solution has lower penetration power for staining large specimens even for a longer period. If a more highly concentrated solution, for instance 3%, was used throughout the whole process, the time to reach a staining effect

would only take half the duration taken here (Fig. 5). On the other hand, if only 1% iodine solution was used over the same duration, the final iodine concentration would be only half the value of our experiment. However, a high concentration can lead to high degree of tissue shrinkage. Considering the combined experimental and simulation data, progressive replenishment and enrichment of solution (e.g., from 1% to 3%) appears to be an effective way (compared to using only 2%) to achieve a compromise between an ideal staining effect and tissue distortion. But this conclusion is not evident from our simulation; the higher contrasting effect in *P. subis* is remarkable in comparison with that of *M. aurifrons.*

Through a successive replacement of solution, different grayscale increases can be compared among various tissues, especially for bones versus muscles. Due to the heterogeneous size of different segments of the avian body, e.g., cephalic material versus the pectoral region, committing to one concentration or protocol for the whole specimen might not be a panacea. For example, cranial tissues and wing muscles were stained effectively in the first stage with a concentration of 1% (Fig. 3) in the *P. subis* specimen and 2% for the *M. aurifrons* specimen, but the pectoral region was insufficiently stained (Fig. 3) in both. Therefore, the priority of which tissues or which sub-region of the samples to investigate plays a role in the designing the staining protocol. Otherwise, step-wise staining and serial scanning may be used to ensure that all sub-regions of the specimen can be imaged well.

The mismatch of staining results may reflect a practical difficulty in staining large-sized bird specimen, a phenomenon that has been observed previously (Li et al., 2015; Gignac et al., 2016). Adult birds are particularly resistant to iodine penetration in staining because of the thick feathered covering and large muscle mass, especially in the pectoral region. In addition, the highly stained feathers indicate high adsorption of iodine by these exterior layers. These factors might lead to a different outcome between experiments and the modeling analysis. The situation may be alleviated by raising the concentration of iodine solution in a step-wise pattern, which was applied in the *P. subis* staining. However, we cannot totally rule out model misfit; for instance, the simulation here used two-dimensional analyses to simplify a real three-dimensional volume object. Although the measured sternal depth is deeper in *P. subis* the width and volume of the sternal muscles in *M. aurifrons* could be larger and required more iodine for an adequate staining. It is also possible that subtle differences in specimen preparation could affect the uptake rate or the maximum amount of iodine that can be absorbed in various tissues, which would create a limiting condition not implemented in our simplified modeling.

Iodine adsorption rate significantly differs between the bone and soft tissues (Li et al., 2015, 2016). When lower iodine concentrations were used, the bone was hardly stained compared to soft tissues (Fig. 1). With raised concentrations, bones start to be stained in a fashion similar to the soft tissues. We thus find concentration of the staining solution to be the key to retaining a high X-ray contrast density between bone and soft tissues. Bones are much higher in X-ray attenuation than soft-tissues before staining. While low concentrated iodine solution was applied

($\leq$2%), muscular tissues slightly increased in grayscale values, but hardly exceed that of the bone they surrounded (Figs. 2, 3). Over long staining periods (e.g., over a month), when 2%–3% concentration was used, soft tissue grayscale values started to exceed that of the surrounding bones. Accurate control of the final staining effect within soft tissue (i.e., less than 300 mmol/l) is thus the key to optimizing the contrast of bone versus soft tissues. The structure and chemical composition of the bone versus muscles may explain the distinct pattern observed, but further analyses are needed to explain the apparent existence of a minimal value or a threshold value for staining bony tissues.

5. Conclusion and caveats

For imaging anatomy in whole avian specimens, our study provides potential insights into optimization of the staining procedure. Through modeling, a relationship between duration and iodine concentration was established in the three sampled birds (Fig. 5). This relationship held for the whole bird specimen and individual muscles. Within the small-sized forearm and the cranial muscle, a short duration of staining works well as shown in the *A. alexandri* specimen (16 days). For larger muscle masses than those with a cross-section longer than 1 cm, a longer staining period combined with a continuous replacement of higher concentration is encouraged. Although different taxa were used in this study, a similar 'K_m' was effective in explaining the staining variations for all experiments. Similar tissue types and arrangements can be a potential explanation of these results.

Feathers of birds comprise an initial hydrophobic barrier that adsorbs a large amount of iodine. In comparison, the cornified scales of squamates and alligators, and the hairs of mammals (Gignac et al., 2016) all have variable external layers with higher permeability (Metscher, 2009a, 2009b; Preininger et al., 2016). The larger specimens in this study stained less evenly and took longer to stain than the smaller specimen. In the case of shorter staining times, *P. subis* and *M. aurifrons* both have a good fit with the model predictions. For longer staining periods, the fit of model to experimental data is less ideal for the second stage of staining. The integument of birds might be a factor that contributes to the inconsistency of lower grayscales in experiments compared to the higher values in the simulation. Therefore, removing the integument may be a choice for practical considerations if only the internal anatomy of a bird specimen is targeted. Improvements in the models used and model parameters may still be needed. These caveats should be kept in mind when other researchers consider following the protocol used here.

Appendix A. Supplementary data

Supplementary data associated with this article can be found, in the online version, at https://doi.org/10.1016/j.palwor.2018.10.004.

References

Aslanidi, O.V., Nikolaidou, T., Zhao, J., Smaill, B.H., Gilbert, S.H., Holden, A.V., Lowe, T., Withers, P.J., Stephenson, R.S., Jarvis, J.C., Hancox, J.C., Boyett, M.R., Zhang, H., 2013. Application of micro-computed tomography with iodine staining to cardiac imaging, segmentation, and computation model development. IEEE Transactions on Medical Imaging 32, 8–17.

Cussler, E.L., 2009. Diffusion: Mass Transfer in Fluid Systems. Cambridge University Press, Cambridge, 647 pp.

Degenhardt, K., Wright, A.C., Horng, D., Padmanabhan, A., Epstein, J.A., 2010. Rapid 3D phenotyping of cardiovascular development in mouse embryos by micro-CT with iodine staining circulation. Cardiovascular Imaging 3, 314–322.

Diogo, R., Abdala, V., 2010. Muscles of Vertebrates. CRC Press, Boca Raton, 500 pp.

Faulwetter, S., Vasileiadou, A., Kouratoras, M., Dailianis, T., Arvanitidis, C., 2013. Micro-computed tomography: introducing new dimensions to taxonomy. ZooKeys 263, 1–45.

Gignac, P.M., Kley, N.J., 2014. Iodine-enhanced micro-CT imaging: methodological refinements for the study of the soft-tissue anatomy of post-embryonic vertebrates. Journal of Experimental Zoology Part B: Molecular and Developmental 322, 166–176.

Gignac, P.M., Kley, N.J., Clarke, J.A., Colbert, M.W., Morhardt, A.C., Cerio, D., Cost, I.N., Cox, P.G., Daza, J.D., Early, C.M., Echols, M.S., Henkelman, R.M., Herdina, A.N., Holliday, C.M., Li, Z., Mahlow, K., Merchant, S., Müller, J., Orsbon, C.P., Paluh, D.J., Thies, M.L., Tsai, H.P., Witmer, L.M., 2016. Diffusible iodine-based contrast-enhanced computed tomography (diceCT): an emerging tool for rapid, high-resolution, 3-D imaging of metazoan soft tissues. Journal of Anatomy 228, 889–909.

Herdina, A.N., Plenk Jr., H., Benda, P., Lina, P.H., Herzig-Straschil, B., Hilgers, H., Metscher, B.D., 2015. Correlative 3D imaging of *Pipistrellus* penis micromorphology: validating quantitative microCT images with undecalcified serial ground section histomorphology. Journal of Morphology 276, 695–706.

Hopwood, D., 2002. Fixation and fixatives. In: Gamble, M., Bancroft, J.D. (Eds.), Theory and Practice of Histological Techniques, 5th Edition. Elsevier Health Sciences, Churchill Livingstone, Edinburgh, pp. 63–84.

Holliday, C.M., Tsai, H.P., Skiljan, R.J., George, I.D., Pathan, S., 2013. A 3-D interactive model and atlas of the jaw musculature of *Alligator mississippiensis*. PLoS One 8, e62806, http://dx.doi.org/10.1371/journal.pone.0062806.

Jeffery, N.S., Stephenson, R.S., Gallagher, J.A., Jarvis, J.C., Cox, P.G., 2011. Microcomputed tomography with iodine staining resolves the arrangement of muscle fibres. Journal of Biomechanics 44, 189–192.

Kevorkian, J., 1990. Partial Differential Equations: Analytical Solution. Springer, My Copy UK, 564 pp.

Kupczik, K., Stark, H., Mundry, R., Neininger, F.T., Heidlauf, T., Röhrle, O., 2015. Reconstruction of muscle fascicle architecture from iodine-enhanced microCT images: a combined texture mapping and streamline approach. Journal of Theoretical Biology 382, 34–43.

Lecker, D.N., Kumari, S., Khan, A., 1997. Iodine binding capacity and iodine binding energy of glycogen. Journal of Polymer Science 35, 1409–1412.

Li, Z., Clarke, J.A., Ketcham, R.A., Colbert, W.M., Yan, F., 2015. An investigation of the efficacy and mechanism of contrast-enhanced X-ray computed tomography utilizing iodine for large specimens through experimental and simulation approaches. BMC Physiology 15, 5.

Li, Z., Ketcham, R.A., Yan, F., Maisano, J.A., Clarke, J.A., 2016. Comparison and evaluation of the effectiveness of two approaches of diffusible iodine-based contrast-enhanced computed tomography (diceCT) for avian cephalic material. Journal of Experimental Zoology Part B: Molecular and Developmental 326 (6), 352–362.

Metscher, B.D., 2009a. Micro-CT for comparative morphology: simple staining methods allow high-contrast 3-D imaging of diverse nonmineralized animal tissues. BMC Physiology 9, 11.

Metscher, B.D., 2009b. Micro-CT for developmental biology: a versatile tool for high-contrast 3-D imaging at histological resolutions. Developmental Dynamics 238, 632–640.

Preininger, D., Handschuh, S., Boeckle, M., Sztatecsny, M., Hödl, W., 2016. Comparison of female and male vocalisation and larynx morphology in the size dimorphic foot-flagging frog species *Staurois guttatus*. Journal of Herpetology 26 (3), 187–197.

Tahara, R., Larsson, H.C., 2013. Quantitative analysis of microscopic X-ray computed tomography imaging: Japanese quail embryonic soft tissues with iodine staining. Journal of Anatomy 223, 297–310.

Wong, M.D., Spring, S., Henkelman, R.M., 2013. Structural stabilization of tissue for embryo phenotyping using micro-CT with iodine staining. PLoS One 8, e84321, http://dx.doi.org/10.1371/journal.pone.0084321.

Vickerton, P., Jarvis, J., Jeffery, N., 2013. Concentration-dependent specimen shrinkage in iodine-enhanced microCT. Journal of Anatomy 22 (3), 185–193.